

## Target dependence of central rapidity $\Lambda$ production in sulfur-nucleus collisions at 200 GeV/c per nucleon

E. Andersen,<sup>(1)</sup> P. D. Barnes,<sup>(8)</sup> R. Blaes,<sup>(10)</sup> H. Braun,<sup>(10)</sup> J. M. Brom,<sup>(10)</sup> B. Castaño,<sup>(9),\*</sup> M. Cherney,<sup>(7)</sup> M. Cohler,<sup>(12)</sup> B. de la Cruz,<sup>(6)</sup> G. E. Diebold,<sup>(8),†</sup> C. Fernández,<sup>(9)</sup> G. Franklin,<sup>(8)</sup> C. Garabatos,<sup>(9)</sup> J. A. Garzón,<sup>(9)</sup> W. M. Geist,<sup>(10)</sup> D. Greiner,<sup>(2)</sup> C. Gruhn,<sup>(2)</sup> M. Hafidouni,<sup>(10)</sup> J. Hrubec,<sup>(11)</sup> D. Huss,<sup>(10)</sup> J. L. Jacquot,<sup>(10)</sup> P. G. Jones,<sup>(3)</sup> J. P. M. Kuipers,<sup>(4,12),\*\*</sup> M. Ladrem,<sup>(10)</sup> P. Ladrón de Guevara,<sup>(6)</sup> D. Liko,<sup>(11)</sup> S. Lopez-Ponte,<sup>(9)</sup> G. Løvholden,<sup>(1)</sup> J. MacNaughton,<sup>(11)</sup> C. J. Maher,<sup>(8)</sup> A. Michalon,<sup>(10)</sup> M. E. Michalon-Mentzer,<sup>(10)</sup> J. Mosquera,<sup>(9)</sup> Z. Natkaniec,<sup>(5,2)</sup> J. M. Nelson,<sup>(3)</sup> G. Neuhofer,<sup>(11)</sup> C. Perez de los Heros,<sup>(6)</sup> M. Pló,<sup>(9)</sup> P. Porth,<sup>(11)</sup> B. Powell,<sup>(4)</sup> B. Quinn,<sup>(8)</sup> A. Ramil,<sup>(9)</sup> J. L. Riester,<sup>(10)</sup> H. Rohringer,<sup>(11)</sup> G. Sakrejda,<sup>(5)</sup> I. Sakrejda,<sup>(8,10,11),‡</sup> T. Thorsteinsen,<sup>(1)</sup> J. Traxler,<sup>(11)</sup> C. Voltolini,<sup>(10)</sup> A. Yañez,<sup>(9)</sup> P. Yepes,<sup>(9),§</sup> and R. Zybent<sup>(3)</sup>

(NA36 Collaboration)

<sup>(1)</sup>University of Bergen, Department of Physics, N-5007 Bergen, Norway

<sup>(2)</sup>Lawrence Berkeley Laboratory, Berkeley, California 94720

<sup>(3)</sup>University of Birmingham, Department of Physics, Birmingham B15 2TT, United Kingdom

<sup>(4)</sup>European Organization for Nuclear Research (CERN), CH-1211 Geneva 23, Switzerland

<sup>(5)</sup>Instytut Fizyki Jadrowej, PL-30 055 Krakow 30, Poland

<sup>(6)</sup>CIEMAT, Division de Física de Partículas, E-28040 Madrid, Spain

<sup>(7)</sup>Creighton University, Department of Physics, Omaha, Nebraska 68178

<sup>(8)</sup>Carnegie-Mellon University, Department of Physics, Pittsburgh, Pennsylvania 15213

<sup>(9)</sup>Universidad de Santiago Departamento Física de Partículas, E-15706 Santiago de Compostela, Spain

<sup>(10)</sup>Centre de Recherches Nucléaires, Institut National de Physique Nucléaire et de Physique des Particules, Université L. Pasteur, Boîte Postal 20, F 67037 Strasbourg, France

<sup>(11)</sup>Institut für Hochenergiephysik (HEPHY), A-1050 Wien, Austria

<sup>(12)</sup>University of York, Department of Physics, York YO1 5DD, United Kingdom

(Received 26 December 1991)

Central rapidity  $\Lambda$  production has been measured in sulfur collisions with Cu, Ag, and Pb at 200 GeV/c per nucleon. Lambdas produced in these collisions were identified by their charged decays recorded by a time projection chamber. The  $\Lambda$  yields are compared as a function of target mass. For each target, the yields are reported as a function of  $\Lambda$  transverse kinetic energy and zero degree energy (a measure of collision centrality). In each system, the data exceed predictions of the VENUS (4.02) model of sulfur-nucleus collisions. The observed excesses show no obvious variation with collision centrality from moderate to highly central collisions.

PACS number(s): 25.75.+r

### I. INTRODUCTION

A new state of hadronic matter, called quark-gluon plasma (QGP), has been hypothesized to form under conditions of extreme heating and/or compression [1,2]. In the violent collisions of large nuclei at high energies, it is possible that suitable conditions may be reached in which

this new state of hadronic matter may form. This possibility has spurred a great deal of experimental and theoretical activity in an effort to verify the formation of QGP in nucleus-nucleus collisions. Toward this end enhanced strange particle production has been suggested as a possible indicator of QGP formation in relativistic nucleus-nucleus collisions [3].

Motivated by this, CERN experiment NA36 has pursued an experimental study of strange particle production in collisions of 200 GeV/c per nucleon sulfur ions with nuclear targets. This paper presents a measurement of  $\Lambda$  production based on the analysis of data recorded in October 1987 during the first sulfur ion running for the NA36 experiment. At that time data from sulfur collisions with Cu, Ag, and Pb target nuclei were recorded simultaneously. For this measurement only  $\Lambda$ 's produced with laboratory rapidity  $y_{\text{lab}}$  in the range  $2.0 < y_{\text{lab}} < 4.0$  and transverse momentum  $p_T > 0.5$  GeV/c are considered.

\*Now at I. B. San Sebastian de los Reyes II, San Sebastian/de los Reyes, Madrid, Spain.

†Now at Yale University, Physics Department, New Haven, CT 06511.

‡Now at Lawrence Berkeley Laboratory, Berkeley, CA 94720.

§Now at McGill University, Montréal, Quebec, Canada H3C 3J7.

\*\*Now at University of Freiburg, Hermann-Herder-Strasse 3, D-7800 Freiburg, Germany.

## II. EXPERIMENTAL APPARATUS

Sulfur ions were accelerated to 200 GeV/ $c$  per nucleon by the CERN Super Proton Synchrotron and delivered to the NA36 experiment via the H2 beam line. The arrival of each beam particle was signaled by a plastic scintillator “start” counter, while three multiwire proportional chambers (MWPC’s) were used to measure precisely the incident beam trajectories. The beam spot on target (approximately 0.5 cm $\times$ 1.0 cm) was defined by two remote-controlled beam geometry scintillator stations, which were also used to veto events accompanied by beam halo.

The target region of the 1987 NA36 experimental layout is shown in Fig. 1. As beam particles entered the target region, sulfur ions were identified by their charge  $Z$ , measured by a thin (500  $\mu$ m) Si counter called the beam tag (BT). Three target foils (Pb, Ag, and Cu) of 0.01 interaction length were simultaneously placed in the target region at 9-cm intervals. The BT was positioned 4 cm upstream of the first target foil. A second Si counter, called the beam veto (BV), was placed 9 cm downstream of the last target foil and was used to veto events in which a particle with  $Z \geq 15$  exited the target region, indicating that no severe nuclear interaction had occurred.

The principle detector of the NA36 experiment was a time projection chamber (TPC) [4], which was used to record three-dimensional space points on charged particle trajectories. The active TPC volume measured 1.0 m $\times$ 0.5 m $\times$ 0.5 m and was filled with Ar-CH<sub>4</sub> (9%). The TPC was centered in the upper half of a large superconducting dipole magnet M1, which was operated at a central field of 2.7 T. In this position the beam axis passed approximately 2 cm below the lower edge of the active TPC volume, and the Cu, Ag, and Pb targets were located 117, 126, and 135 cm upstream of its front edge. This experimental configuration minimized the number of tracks in the TPC, which were unrelated to strange particle decays (e.g., low-momentum pions and noninteracting nuclear fragments). To optimize the TPC acceptance for  $\Lambda$  decay products, the main component of the magnetic field was oriented to bend positive tracks in the negative  $y$  direction (i.e., downward) to match the topological (momentum) asymmetry of the  $\Lambda$  decay products.

Downstream of the TPC were several detector systems formerly part of the European Hybrid Spectrometer [5]. These included large MWPC’s and drift chambers, a gas Cerenkov counter, and electromagnetic and hadronic calorimetry, which were used for triggering and event characterization.

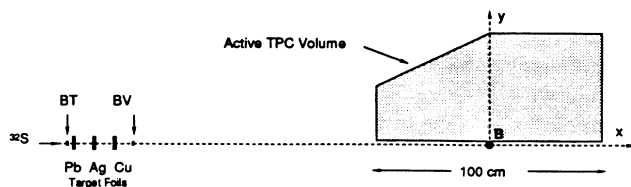


FIG. 1. 1987 NA36 experimental setup showing the target region and TPC.

## III. DATA ANALYSIS

### A. TPC event reconstruction

In the first stage of event reconstruction, three-dimensional space points were reconstructed along charged particle trajectories inside the TPC. Under the influence of a uniform electric field of approximately 100 V/cm, ionization in the TPC from such trajectories was drifted to the TPC end cap, where it was amplified and collected by short (12-mm-long) sense wires arranged in a two-dimensional ( $x,y$ ) array. The time at which any of the 6400 sense wires produced a signal above a set threshold was recorded by pipeline time-to-digital converters. Based on the ( $x,y$ ) position of the sense wires and the recorded drift time, unambiguous three-dimensional space points along the trajectories could be determined by integrating the charge transport equation [6] describing electron drift in the presence of electric and magnetic fields.

For NA36 this task was complicated by the nonuniformity of the M1 magnetic field, which resulted in an electron drift velocity that varied with position in both magnitude and direction. Because of the large cyclotron frequency for electrons drifting in the Ar-CH<sub>4</sub> gas mixture, ionization produced in the TPC drifted along paths which predominantly followed magnetic field lines. These drift paths deviated by as much as 1–2 cm from simple straight lines to the end cap. Nonetheless, accurate three-dimensional space points were obtained by numerically integrating the electron drift velocity under the influence of the nonuniform M1 field.

From the three-dimensional space point information, charged particle trajectories were reconstructed in the TPC. The pattern recognition procedure used was based on a track following method adapted from the ALEPH experiment at LEP [7]. Because of low TPC hit efficiency ( $\approx 40\%$ ) during the 1987 running, the ALEPH algorithm required substantial development to provide acceptable event reconstruction. The algorithm proceeded as follows: Starting at the downstream end of the TPC, pairs of space points were extrapolated upstream as possible track segments in search of additional hits lying along the same general trajectory. As additional space points were found and added to a track segment, the extrapolation was refined and repeated. Once all suitable space points were found for a given track, the points were fit using a least-squares minimization procedure of the particle trajectory in the M1 magnetic field. The results of the track fit yielded the particle charge, momentum, and errors.

### B. Target identification

As three target foils were used simultaneously in the experiment, the reconstructed tracks in the TPC were needed to identify the target foil in which a particular interaction occurred. By extrapolating TPC tracks to the target region through the known magnetic field, the position of the primary interaction vertex could be reconstructed. In the target region, the magnetic field is low, and so particle trajectories are approximately straight lines, especially in the nonbend plane projection ( $x,z$ ).

TABLE I. Target identification cuts, number of events per target, and approximate contamination of each target sample from primary interactions in surrounding air, adjacent foils, and trigger counters BT and BV.

Target	$x_0$ range (cm)	No. of events	BT	Approx. % contamination from				
				Pb	Ag	Cu	BV	Air
Pb	$-189.5 < x_0 < -180.5$	37 185	1		2	0	0	1
Ag	$-180.5 < x_0 < -171.5$	32 459	0	2		2	0	1
Cu	$-171.5 < x_0 < -162.5$	25 370	0	0	2		0	1

Working in this projection, the extended tracks were fit as a set of lines passing through a common point  $(x_0, z_0)$ . The value of  $(x_0, z_0)$  which best fit the set of extended tracks for each event was taken to be the position of the primary interaction vertex.

Figure 2 shows the  $x_0$  distribution of reconstructed primary interaction vertices. Clear peaks are seen along the beam axis at the positions of the three target foils. The tails to either side of the target foil peaks are due to primary interactions in the BT and BV counters, which failed to self-veto, as well as to interactions with the air in the target region. The width of each peak obtained from a multiple Gaussian fit yields a resolution of  $\sigma_x \approx 2.3$  cm. Slightly better results ( $\sigma_x \approx 2.0$  cm) have been obtained using a Kalman filter algorithm [8]; however, this was not used in the present analysis.

To associate a given event with a particular target foil, cuts were placed at  $\pm 4.5$  cm from the centroids of the peaks of Fig. 2. These cuts and the statistics of the event sample obtained for each target are listed in Table I. While the primary vertex resolution is not sufficient to separate unambiguously all events from adjacent targets, the contamination of the event samples from primary interactions originating in adjacent targets is small and is summarized in Table I.

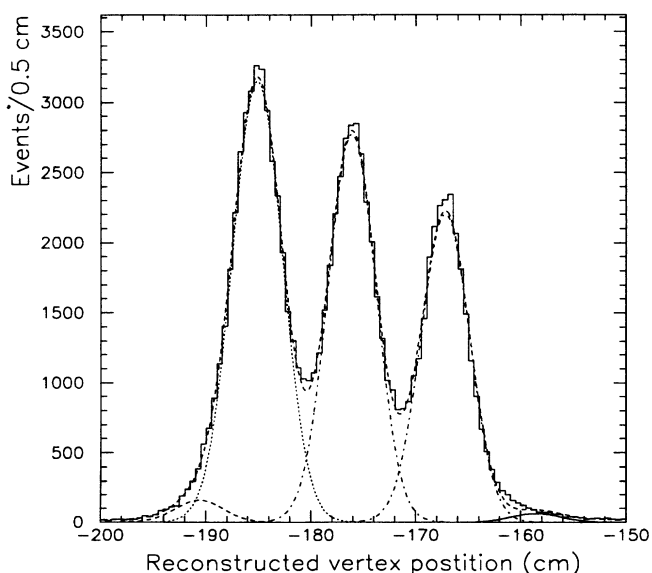


FIG. 2. Distribution of the  $x$  position of the reconstructed primary interaction vertices. The positive  $x$  axis is in the beam direction, and the origin is at the center of the M1 magnet.

### C. Trigger and event characterization

In a simple geometric picture of the collision process, the average number of noninteracting or spectator nucleons from the projectile decreases with impact parameter. After the collision the spectator nucleons from the projectile largely continue along the beam axis. As a result, one can estimate the number of such projectile spectator nucleons in a given collision, and hence the collision centrality, by measuring the energy of all particles emerging near zero degrees with respect to the beam axis. For NA36 this zero degree energy  $E_0$  was measured by the forward neutral calorimeter (FNC) [5].

The FNC consisted of 200 Fe-scintillator sandwich-type calorimeter blocks ( $144 \times 15 \times 15$  cm<sup>3</sup>) arranged in a  $10 \times 20$  block wall and positioned such that projectile fragments within approximately  $0.4^\circ$  of the beam axis were detected in the four central blocks. This near-zero-degree energy measurement was used for triggering and event characterization. In particular, the zero degree energy measured by FNC was used on line to define a central collision trigger. For the present data set, the selection of events written to tape was obtained from a mix of beam (BEAM), minimum bias (MINBIAS), and central collision (CENTRAL) triggers. The BEAM trigger only required that a charged beam particle enter the target region and was downscaled by a factor of 512 (i.e., only one in every 512 BEAM triggers were recorded to tape). For MINBIAS triggers an incident  $Z = 16$  ion was required to satisfy the BEAM trigger and appear to undergo a charge-changing interaction in the target region defined by BT and BV. This trigger was downscaled by a factor of 128. Finally, the CENTRAL collision trigger required a MINBIAS trigger in which less than about 3800 GeV was deposited in the central FNC blocks (slightly more than half the beam energy). This  $E_0$  threshold, which made for a rather loose central interaction requirement, was selected to saturate the data-acquisition system for the relatively low beam flux on target ( $\approx 10$  kHz). The interaction cross sections for the CENTRAL trigger were 0.8, 1.3, and 2.2 b for sulfur collisions with the Cu, Ag, and Pb targets, respectively.

For the MINBIAS data set, differential interaction cross sections  $d\sigma/dE_0$  have been measured for each target as a function of  $E_0$ . These cross sections are shown in Fig. 3(a). Note the differences in the falloff of the differential cross section for each target as  $E_0$  approaches zero. The value of  $E_0$  at which the cross sections vanish is observed to decrease with increasing target atomic mass as a result of greater stopping power of the thicker target nuclei. A second geometric effect is the ‘‘pileup’’

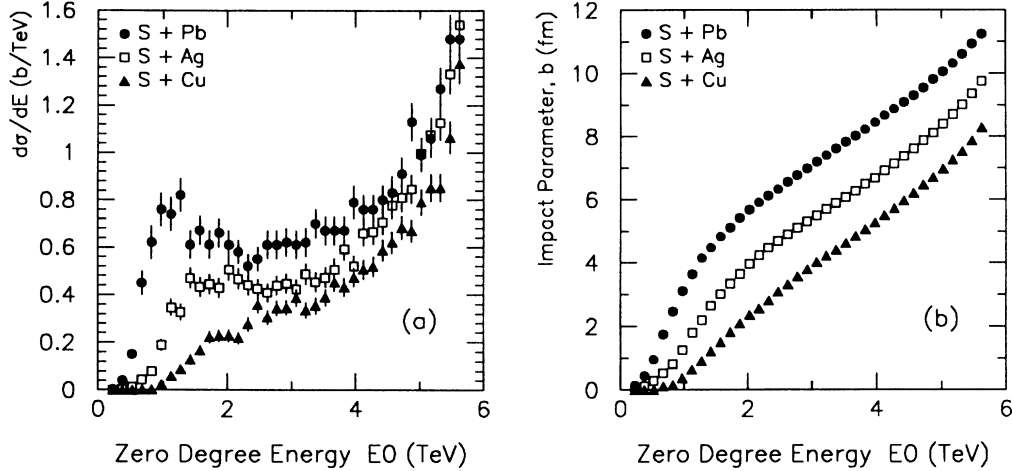


FIG. 3. (a) Differential interaction cross sections for S+Cu, Ag, and Pb collisions as a function of zero degree energy  $E_0$ , measured by FNC. (b) Effective impact parameter as a function of  $E_0$  for S+Cu, Ag, and Pb collisions.

in the S+Pb differential cross section around  $E_0=1$  TeV. This results from little change in the thickness of the Pb nucleus presented to the sulfur projectile near zero impact parameter. Consequently, there is a range of small impact parameters which result in nearly the same average  $E_0$ . Similar behavior has also been reported by WA80 [9].

Within a simple geometric-overlap model of the inelastic nucleus-nucleus interaction, the effective monotonic relationship between  $E_0$  and the impact parameter  $b$  may be determined from the differential interaction cross section  $d\sigma/dE_0$ . For events with  $E_0=E$ , the corresponding effective impact parameter  $b(E)$  may be determined from the relation

$$\pi b(E)^2 = \int_0^E \frac{d\sigma}{dE_0} dE_0. \quad (1)$$

By integrating the cross sections of Fig. 3(a) in this manner, a correlation between effective impact parameter and the  $E_0$  measured by the central FNC blocks was obtained for each target. These are plotted in Fig. 3(b). In this approach the CENTRAL collision trigger ( $E_0 < 3800$  GeV) effectively selected maximum impact parameters of approximately 5.0, 6.4, and 8.3 fm for the Cu, Ag, and Pb targets, respectively. These maximum impact parameters roughly correspond to the radii of the target nuclei. This implies a minimum collision overlap of approximately half of the sulfur projectile, which is consistent with the maximum  $E_0$  for the CENTRAL trigger of slightly more than half of the beam energy.

#### D. Lambda identification and analysis

Lambdas produced in the sulfur-nucleus collisions were identified by the characteristic topology of their decay products (i.e.,  $\Lambda \rightarrow p\pi^-$ ) recorded by the TPC. The charged tracks originating from the decay vertex form a so-called neutral vee or  $V^0$ . Based on the measured momenta of the decay products, the likely identity of the

parent particle was determined by invariant mass calculation.

From the reconstructed TPC tracks,  $\Lambda$  decay candidates were selected from oppositely charged pairs which appeared to share a common vertex within a fiducial decay volume extending 40 cm upstream of the TPC. In order to suppress the contribution of false  $V^0$ s formed by the accidental crossing of two tracks,  $V^0$  candidates were required to have more than a minimum length (20 cm) and number of hits per track (seven or eight for the negative or positive track), have a good topological fit to a  $V^0$  decay ( $\chi^2/D.F. < 2.0$ ), have a total  $V^0$  momentum vector which is consistent with originating from the primary interaction (within  $1.75\sigma$ ), and have more than a minimum two-track separation (1.0 cm) when the decay tracks were extrapolated to the target. Note that these cuts apply equally to all  $V^0$ s, regardless of mass, and therefore do not bias a particular reconstructed  $V^0$  mass.

As the identities of the decay products were not known (no  $dE/dx$  information was recorded for particle identification in the TPC), there is some ambiguity between  $V^0$ s from  $\Lambda \rightarrow p\pi^-$  decays and those from the decays of  $K_s^0 \rightarrow \pi^+\pi^-$ . Fortunately, the kinematic overlap of these two decays is limited and may largely be excluded by an appropriate cut in the phase space of the decay products. A convenient variable for this purpose is the longitudinal momentum asymmetry of the decay [10],  $\alpha$ , defined as

$$\alpha = \frac{p_L^+ - p_L^-}{p_L^+ + p_L^-}. \quad (2)$$

Here  $p_L^+$  and  $p_L^-$  refer to the longitudinal momentum components (along the total momentum vector of the  $V^0$ ) of the positively and negatively charged decay product, respectively. The phase space for  $\Lambda \rightarrow p\pi^-$  decays is largely limited to values of  $\alpha > 0.5$ , with an average value of 0.7, because of the asymmetric momentum sharing between the decay  $p$  and  $\pi^-$  due to their mass difference. On the other hand, the  $K_s^0 \rightarrow \pi^+\pi^-$  decays fall predom-

inantly in the range  $|\alpha| < 0.5$  with an average value of zero.

The solid curve in Fig. 4(a) shows the invariant  $M(p, \pi^-)$  mass for all  $V^0$  candidates with  $\alpha > 0.5$  and passing background suppression cuts. In this distribution a peak near the  $\Lambda$  mass ( $M_\Lambda = 1.1156 \text{ GeV}/c^2$ ) is visible, along with significant combinatorial background which survived the cuts. In principle, the cuts could be made more restrictive to suppress the surviving combinatorial background; however, this is not a practical approach as the statistical significance of the measurement suffers considerably in the process. Instead, as discussed below, the remaining combinatorial background was simulated and subtracted from the candidate  $V^0$  distributions. An attempt was made to optimize the background suppression cuts to maximize the net statistical significance of the measurement after background subtraction.

To reproduce the distribution of the combinatorial  $V^0$  background in the data, an event-mixing procedure was employed. In this procedure all positive tracks from one event were combined with all negative tracks from another event originating from the same target and characterized by similar zero degree energy and reconstructed positive and negative track multiplicity. The frequency of a given event type in the mixed event sample was matched to that found in the data. By searching the mixed events for  $V^0$ 's and applying the same cuts as were used for the data, the contribution of combinatorial background was determined for each kinematic distribution of interest. The number of mixed events analyzed in this manner was comparable to the number of events in the data; the precise ratio of the number of mixed events to the number of events in the data was used as the absolute normalization for this procedure. No fit or free parameters were used to force agreement between the combinatorial-background simulation and the data.

As an example of the subtraction procedure, the dashed curve in Fig. 4(a) shows the invariant  $M(p, \pi^-)$  mass distribution of  $V^0$ 's from the combinatorial-background simulation which pass the same cuts used for the data (solid curve). Away from the  $\Lambda$  mass, the agreement between the data and the simulated combinatorial background is excellent. The background-subtracted in-

variant  $M(p, \pi^-)$  mass distribution (obtained from the difference of these two distributions) is shown in Fig. 4(b). A clear peak is seen in this figure at the  $\Lambda$  mass with no evidence of residual combinatorial-background contamination. The mass resolution is found to be about 15  $\text{MeV}/c^2$ , which is compatible with expectations for this data set.

In addition to the background-subtraction procedure, to isolate the raw  $\Lambda$  distributions of interest, cuts were placed on the transverse momentum ( $p_T$ ), rapidity ( $y$ ), reconstructed invariant mass [ $M(p, \pi^-)$ ], and longitudinal momentum asymmetry ( $\alpha$ ) of the  $V^0$  candidates. Additionally, a cut was placed on  $p_\perp$ , which is defined as the momentum component of either decay product transverse to the total momentum vector of the  $V^0$ . These are summarized in Table II. The rapidity and transverse momentum cuts were used to define a kinematic region for  $\Lambda$  production which matched the acceptance of the experimental apparatus. The  $p_\perp$  cut and additional  $\alpha$  cut were used at this point to further avoid regions of the  $\Lambda \rightarrow p\pi^-$  decay phase space that are ambiguous with other physical processes satisfying the neutral vee topology. An example is  $\gamma \rightarrow e^+e^-$  conversions, which tend to have values of  $p_\perp$  very nearly zero. Proceeding in this manner, raw  $\Lambda$  yields as a function of  $p_T$  and  $E0$  were extracted from the data and corrected for combinatorial-background contamination. A summary of the identified yields (before and after background subtraction) is given in Table III.

Acceptance corrections for the raw distributions were calculated by Monte Carlo techniques. For this, a model of the response of the TPC was developed to generate TPC hits for simulated  $\Lambda \rightarrow p\pi^-$  decays. The simulated hits were embedded into real events, which were then analyzed, keeping track of which simulated  $\Lambda$  decays were successfully reconstructed and identified by the standard program of analysis. The acceptance corrections were determined as a function of each kinematic variable of interest (i.e.,  $p_T$  or  $E0$ ) from the ratio of the generated  $\Lambda$  distribution (discussed below) to the correctly identified simulated yield. The  $\Lambda$  decay rate and charged branching ratio were also taken into account. The final corrected  $\Lambda$  distributions were obtained by multiplying the combinatorial background-subtracted distributions by the acceptance corrections calculated in this procedure. This effectively accounts for geometric acceptance and inefficiencies of the experimental apparatus and data analysis procedures.

The rapidities and transverse momenta of the simulated  $\Lambda$ 's were randomly generated according to indepen-

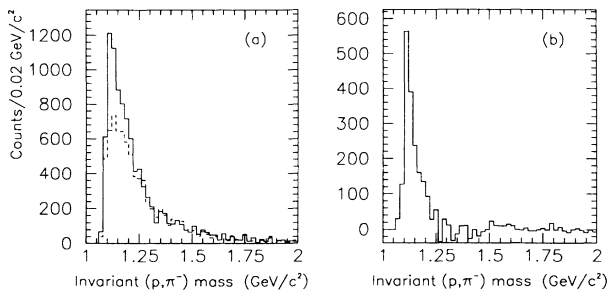


FIG. 4. (a) Invariant  $M(p, \pi^-)$  mass distribution for all  $V^0$  candidates passing background suppression cuts with  $\alpha > 0.5$  (solid curve, data; dashed curve, combinatorial background simulation). (b) The invariant  $M(p, \pi^-)$  mass distribution corrected for combinatorial-background contamination.

TABLE II. Kinematic criteria, in addition to background suppression cuts, required of the  $\Lambda$  sample.

Kinematic variable	Range
Transverse momentum $p_T$	$p_T > 0.5 \text{ GeV}/c$
Rapidity $y$	$2.0 < y_{\text{lab}} < 4.0$
Invariant mass $M(p, \pi^-)$	$1.0806 < M(p, \pi^-) < 1.1506$
$\alpha$	$0.5 < \alpha < 0.85$
$p_\perp$	$0.05 < p_\perp < 0.12 \text{ GeV}/c$

TABLE III. Summary of the statistics of  $V^0$ 's passing all  $\Lambda$  identification and background suppression cuts for both the data and the mixed event sample. Numbers in parentheses are for the CENTRAL event trigger.

Target	No. of real events	No. of mixed events	No. of $\Lambda$ candidates (real events)	No. of $\Lambda$ candidates (mixed events)	No. of $\Lambda$ 's after scaled subtraction
Cu	25 370 (19732)	18 792 (14584)	390 (364)	164 (156)	169 (153)
Ag	32 459 (26832)	24 085 (19868)	598 (580)	267 (257)	238 (232)
Pb	37 185 (32572)	27 586 (24199)	774 (747)	341 (335)	314 (296)
Totals	95 014 (79136)	70 463 (58651)	1762 (1691)	772 (748)	721 (681)

dent input distributions. For this, a linear parameterization was used for the input rapidity distributions, while an exponential in transverse kinetic energy,  $T_T = (p_T^2 + M_\Lambda^2)^{1/2} - M_\Lambda$ , was used to describe the input transverse momentum distributions  $dn/dp_T^2 = Ae^{-T_T/B}$ . The relative number of  $\Lambda$ 's generated per event was determined by the  $E0$  of the event according to a third, a piecewise-linear,  $E0$  input distribution. Since the acceptance corrections as a function of a particular kinematic variable are determined by integrating the acceptance over all other kinematic variables, it is necessary that the simulated  $\Lambda$  distributions agree with the corrected distributions of interest for such a correction scheme to be valid. To achieve this an iterative acceptance correction procedure was employed whereby an initial guess of the  $\Lambda$  yields (as a function of  $y$ ,  $p_T$ , and  $E0$ ) was used for input distributions and the corrected  $\Lambda$  yields from one iteration were used to generate the simulated  $\Lambda$  decays for the following iteration. This correction procedure converged in three iterations and was confirmed in a fourth and final iteration.

As a check of the validity of the  $\Lambda$  identification, background subtraction, and acceptance corrections described in this section, the corrected  $\Lambda$  lifetime distribution is shown in Fig. 5. An exponential fit to the data yields a  $\Lambda$

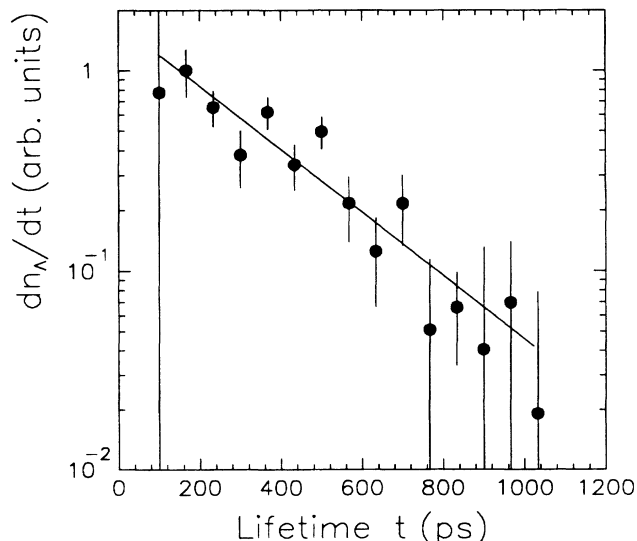


FIG. 5. Corrected  $\Lambda$  lifetime distribution. An exponential fit to the data yields a lifetime of  $276 \pm 56$  ps, in good agreement with the accepted value of 263 ps [11].

lifetime of  $276 \pm 56$  ps, which is in good agreement with the accepted value of 263 ps [11]. Further, the dependence of the corrected  $\Lambda$  yield has been studied as a function of the cuts used for background suppression and  $\Lambda$  identification. It was found that the corrected yield is not significantly affected ( $< 8\%$ ) by reasonable changes in any of the cuts used through the analysis. For example, increasing the required two-track separation of the  $V^0$  decay tracks at the target from 1 to 2 cm resulted in a decrease in the corrected yields of  $2 \pm 5\%$ . Varying the kinematic criteria of Table II (used to isolate the raw  $\Lambda$  sample) by 10–20% resulted in similar statistically insignificant changes in the corrected yields.

#### IV. RESULTS

Correcting for combinatorial-background contamination and acceptance as discussed above,  $\Lambda$  yields are presented in this section as a function of target mass,  $\Lambda$  transverse kinetic energy, zero degree energy, and effective impact parameter. The errors shown are statistical only and reflect the propagation of the uncertainty of the data, the combinatorial-background subtraction, and the experimental acceptance corrections. In addition to the statistical errors shown, the overall systematic uncertainty is estimated to be 25%, stemming primarily from uncertainty in the acceptance corrections. It should be noted that this uncertainty does not reflect the relative target dependence of the  $\Lambda$  yields. Additionally, there are a number of  $K_s^0$  decays which will unavoidably pass the  $\Lambda$  kinematic criteria outlined in Table II. These misidentified decays systematically increase the measured  $\Lambda$  yields by a small fraction. Using the TPC simulation and decay embedding techniques developed for the acceptance correction calculations, the level of this  $K_s^0$  contamination is estimated to be  $3 \pm 1\%$ . The spectra presented here are not corrected for this contamination.

Lambda multiplicity per unit rapidity is shown for CENTRAL triggers in Fig. 6 as a function of target mass. These yields are averaged over the rapidity region  $2.4 < y_{\text{lab}} < 3.6$  and are listed in Table IV. For comparison, predictions of  $\Lambda$  yields have been generated using version 4.02 of the VENUS [12] event generator, which is known to reproduce well  $\Lambda$  production in  $p$ - $p$  collisions. The corresponding  $\Lambda$  multiplicities predicted by VENUS are also listed in Table IV and shown in Fig. 6. The data are found to exceed significantly the VENUS predictions by factors of  $1.9 \pm 0.3$ ,  $2.3 \pm 0.3$ , and  $2.3 \pm 0.3$  for S+Cu, Ag, and Pb collisions, respectively.

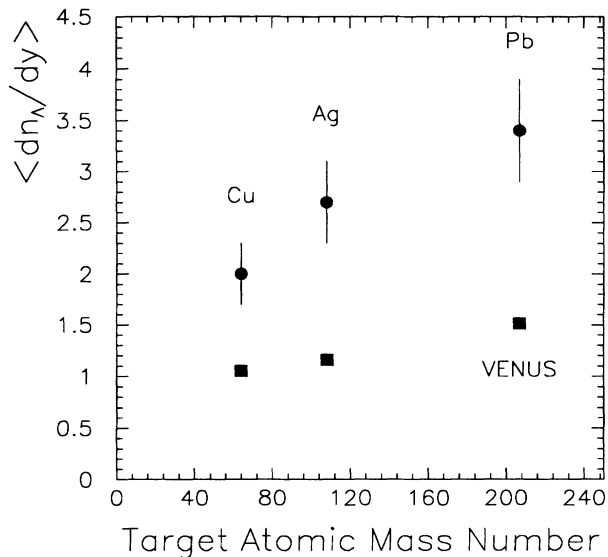


FIG. 6. Average  $\Lambda$  multiplicity per unit rapidity for CENTRAL triggers as a function of target mass. Also shown are predictions of the VENUS model (squares).

Figure 7 shows the corrected  $\Lambda$  yields  $dn/dT_T^2$  per CENTRAL collision trigger, as a function of transverse kinetic energy  $T_T = (p_T^2 + M_\Lambda^2)^{1/2} - M_\Lambda$ , for S+Cu, Ag, and Pb collisions. Fits of the  $T_T$  spectra to the functional form

$$\frac{1}{N_{ev}} \frac{dn}{dT_T^2} = A e^{-T_T/B}, \quad (3)$$

are shown by the solid lines and are found to represent well the data. Parameters of the fits are given in Table IV. Within statistical errors the transverse slope parameter  $B$  for each distribution is found to be independent of the target mass, the target-averaged slope parameter being  $0.227 \pm 0.023$  GeV. At smaller values of  $y_{lab}$ , NA35 has reported similar transverse slopes for  $\Lambda$  production in O+Au ( $B = 0.204 \pm 0.012$  GeV,  $1.5 < y_{lab} < 2.4$ ) [13] and S+S ( $B = 0.194$  GeV,  $0.8 < y_{lab} < 2.0$ ) [14] at the same beam energy per nucleon.

The VENUS predictions of the  $\Lambda$  transverse kinetic energy spectra are also shown in Fig. 7 (dashed curves). These spectra are much flatter than the data and are not well represented by a single exponential in  $T_T$ , which has successfully described the transverse spectra (below a few

GeV/c) of most hadronic species studied in  $A + A'$  collisions at CERN energies [15]. However, it should be noted that for values of  $y_{lab}$  below the range of the present measurement (e.g.,  $y_{lab} < 2.0$ ), the transverse  $\Lambda$  spectra from VENUS become steeper and are in better agreement with  $A e^{-T_T/B}$  behavior.

Finally, the average  $\Lambda$  multiplicity as a function of  $E0$  is shown in Fig. 8 for each target. These distributions include CENTRAL and MINBIAS triggers and therefore span most collision centralities. Also shown is  $\Lambda$  multiplicity as a function of the effective impact parameter determined from the  $E0$  yields and the correlations of Fig. 3(b). Within the statistical significance of the data, no strong target dependence is apparent in the  $\Lambda$  multiplicity produced at fixed  $E0$ . The data do suggest that the  $\Lambda$  multiplicity increases with target mass at fixed effective impact parameters above 4 fm. For impact parameters less than 4 fm, the data are consistent with this behavior, but the statistical significance is not sufficient to make a meaningful statement.

For comparison, VENUS predictions of the  $\Lambda$  yields as a function of impact parameter are shown in Figs. 8(d), 8(e), and 8(f) by the dashed curves. As noted earlier, the predictions fall below measured yields for CENTRAL triggers (i.e.,  $b < 5.0, 6.4,$  and  $8.3$  fm for S+Cu, Ag, and Pb, respectively). Also shown in Figs. 8(d), 8(e), and 8(f) are the predicted yields scaled by the above factors of 1.9, 2.3, and 2.3 to normalize the VENUS predictions to the observed integrated CENTRAL yields for each target. One finds that the measured data and the scaled VENUS predictions are in reasonable agreement as a function of collision centrality.

## V. CONCLUSIONS

A measurement of  $\Lambda$  production at central rapidity has been completed for sulfur collisions with Cu, Ag, and Pb targets. In each of these reactions, data were taken over most collision centralities and a minimum  $\Lambda$  transverse momentum of 0.5 GeV/c was required. For each colliding system, the  $\Lambda$  yields were measured as a function of transverse kinetic energy and zero degree energy, allowing a systematic comparison with model predictions.

The measurements have been compared with predictions of the VENUS event generator (version 4.02), which is found to underpredict the number of  $\Lambda$ 's produced within the kinematic acceptance of this measurement. The CENTRAL data exceed the predictions by factors of

TABLE IV. Parameters of the transverse kinetic energy spectra and average yields per unit rapidity per CENTRAL trigger for  $\Lambda$  production in S+Cu, Ag, and Pb collisions. Also given is the VENUS 4.02 prediction for the average  $\Lambda$  yield per unit rapidity per CENTRAL event.

Target	$\frac{1}{N_{ev}} \frac{dn}{dT_T^2} = A e^{-T_T/B}$		$\left\langle \frac{1}{N_{ev}} \frac{dn}{dy} \right\rangle (2.4 < y_{lab} < 3.6)$	
	$A$ (GeV $^{-2}$ )	$B$ (GeV)	Data	VENUS 4.02
Cu	$8.1 \pm 4.0$	$0.232 \pm 0.047$	$2.0 \pm 0.3$	$1.05 \pm 0.02$
Ag	$13.7 \pm 6.3$	$0.213 \pm 0.037$	$2.7 \pm 0.4$	$1.16 \pm 0.03$
Pb	$15.6 \pm 5.7$	$0.235 \pm 0.034$	$3.4 \pm 0.5$	$1.51 \pm 0.02$

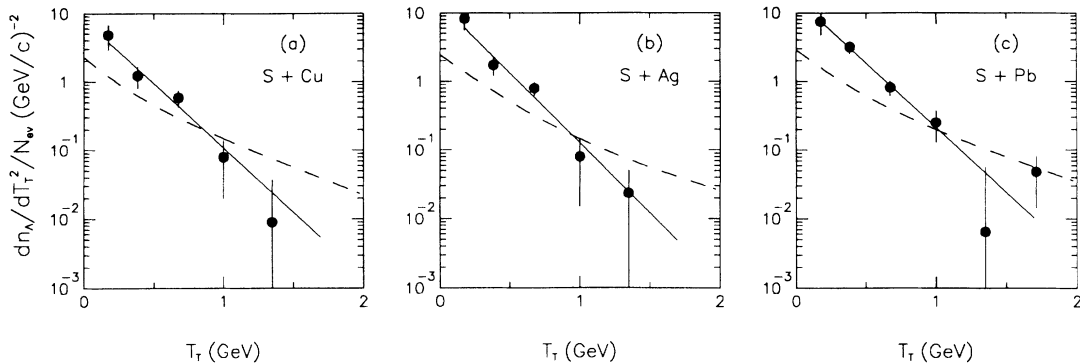


FIG. 7. Lambda yields per CENTRAL event as a function of transverse kinetic energy  $T_T = [(p_T^2 + M_\Lambda^2)^{1/2} - M_\Lambda]$  for sulfur collisions with (a) Cu, (b) Ag, and (c) Pb targets. Dashed curves are predictions of the VENUS model.

$1.9 \pm 0.3$ ,  $2.3 \pm 0.3$ , and  $2.3 \pm 0.3$  for sulfur collisions with Cu, Ag, and Pb targets, respectively. Even with the estimated 25% systematic uncertainty of this measurement, it seems difficult to reconcile the VENUS predictions with the measured yields. In addition to the disagreement in the total  $\Lambda$  yields, the shape of the transverse kinetic energy distributions predicted by the VENUS model differ markedly from the data. The measured  $dn/dT_T^2$  distributions are well represented by a single exponential with an average transverse slope parameter of  $0.227 \pm 0.023$  GeV, which is in reasonable agreement with that found in other measurements of  $\Lambda$  production at CERN energies.

Finally, for the CENTRAL data from each target, VENUS appears to reproduce the shape of the  $\Lambda$  multiplicity as a function of impact parameter, within the statisti-

cal significance of the data. Thus, while a strangeness excess is observed in CENTRAL collisions relative to the VENUS model, the predictions are roughly proportional to the data as a function of impact parameter for these triggers. This is particularly interesting since the VENUS prediction of lambda yield relies on an appropriate superposition of independent nucleon-nucleon collisions without exotic production mechanisms. For  $\Lambda$  production in peripheral collisions (i.e.,  $b > 5.0$ , 6.4, and 8.3 fm for S+Cu, Ag, and Pb, respectively), the statistical significance of the present measurement is not sufficient to draw meaningful conclusions. However, it should be noted that the peripheral-collision lambda yields reported here are not inconsistent with those reported recently by [16].

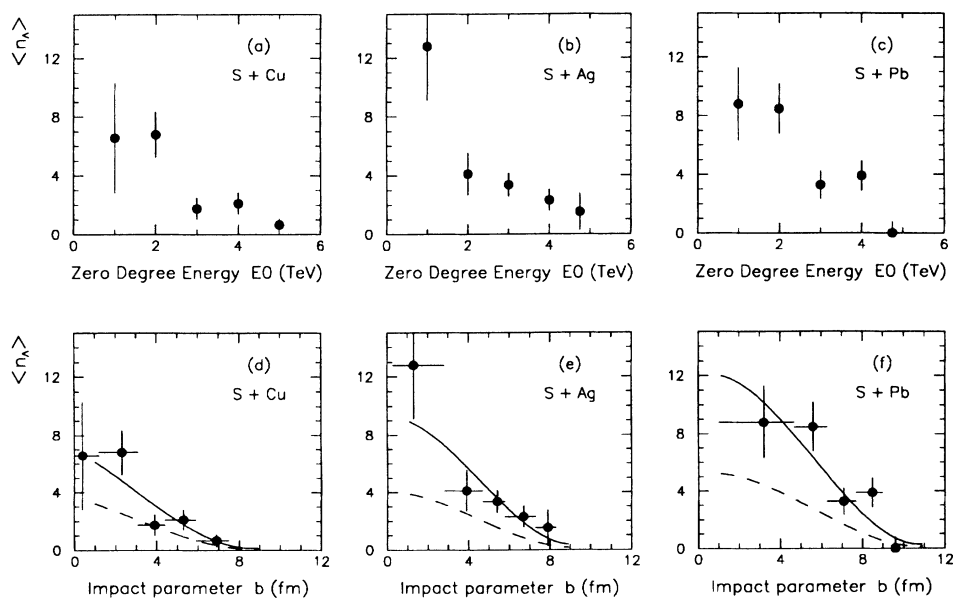


FIG. 8. Lambda yields per event as a function of zero degree energy  $E0$  for sulfur collisions with (a) Cu, (b) Ag, and (c) Pb targets. The yields are also expressed as a function of effective impact parameter in (d), (e), and (f). Horizontal errors reflect the range in effective impact parameter spanned by the constant  $E0$  binning of the data. Dashed curves are predictions of the VENUS model; solid curves are scaled VENUS predictions (see text).

## ACKNOWLEDGMENTS

We would like to thank the CERN EF, SPS, and DD divisions, the H2 beam line group, and the M1 magnet group. We are grateful to Klaus Werner for assistance with the VENUS simulation. This work was supported in

part by CICYT (under Project No. 85-0022, AE86-0031 and No. AE87-0031), by the U.S. Department of Energy [under Contracts No. DE-FG02-87ER40315 (CMU), No. DE-FG02-91ER40652 (Creighton), and No. AC03-76SF00098 (LBL)], and by the Pittsburgh Supercomputing Center (Grant No. PHY890017P).

- 
- [1] N. Cabbibo and G. Parisi, *Phys. Lett.* **59B**, 67 (1975).  
 [2] J. C. Collins and M. J. Perry, *Phys. Rev. Lett.* **34**, 1353 (1975).  
 [3] P. Koch, B. Mueller, and J. Rafelski, *Phys. Rep.* **142**, 167 (1986).  
 [4] C. Garabatos, *Nucl. Instrum. Methods A* **283**, 553 (1989).  
 [5] M. Aguilar-Benitez *et al.*, *Nucl. Instrum. Methods A* **258**, 26 (1987).  
 [6] W. P. Allis, Motions of Ions and Electrons, in *Handbuch der Physik*, edited by S. Flugge (Springer, Berlin, 1956), Vol. 21.  
 [7] W. B. Atwood *et al.*, *Nucl. Instrum. Methods A* **306**, 446 (1991).  
 [8] E. Andersen *et al.*, *Nucl. Instrum. Methods A* **301**, 69 (1991).  
 [9] R. Albrecht *et al.* (WA80), *Phys. Rev. C* **44**, 2736 (1991).  
 [10] J. Podolanski and R. Armenteros, *Philos. Mag.* **45**, 13 (1954).  
 [11] M. Aguilar-Benitez *et al.*, *Phys. Lett. B* **239** (1990).  
 [12] K. Werner, *Z. Phys. C* **42**, 85 (1989). For the VENUS 4.02 simulation, the following (default) values of the most important VENUS parameters were used:  
 KZENTR=9 (Fermi gas entropy treatment cutoff)  
 TAUNLL=1.0 fm/c (cluster lifetime)  
 TAUREA=1.4 fm/c [reaction (formation) time]  
 AMSAIC=0.8 GeV (string-string interaction cutoff mass)  
 RADIAC=1.5 fm (baryon diameter)  
 RADIUS=0.7 fm (meson diameter)  
 [13] A. Bamberger *et al.* (NA35), *Z. Phys. C* **43**, 25 (1989).  
 [14] J. Bartke *et al.* (NA35), *Z. Phys. C* **48**, 191 (1990).  
 [15] J. Schukraft, Report No. CERN-PPE/91-04, 1991.  
 [16] E. Andersen *et al.* (NA36), in Proceedings of the Quark Matter '91 Conference, Gatlinburg, TN, 1991, *Nucl. Phys. A* (to be published).

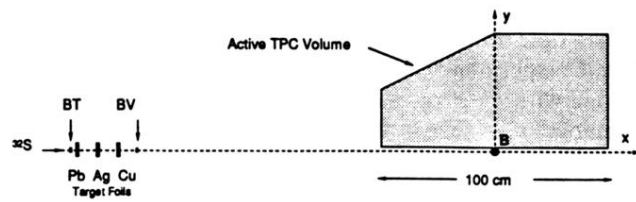


FIG. 1. 1987 NA36 experimental setup showing the target region and TPC.